The Astrophysical Journal Letters, 996:L38 (15pp), 2026 January 10 https://doi.org/10.3847/2041-8213/ae2a20

GRB 250704B: An Off-axis Short GRB with a Long-lived Afterglow Plateau

Vishwajeet Swain[1,19], Tomás Ahumada[2,19], Sameer K. Patil[1], Yogesh Wagh[1], Varun Bhalerao[1], Ehud Nakar[3], Mansi Kasliwal[2], Xander J. Hall[4], Malte Busmann[5], Utkarsh Pathak[1], Shreya Anand[6,7,20], Viraj Karambelkar[2], Igor Andreoni[8], G. C. Anupama[9], Anuraag Arya[1], Arvind Balasubramanian[9], Sudhanshu Barway[9], Jonathan Carney[10], Michael Coughlin[11], D. Eappachen[9], James Freeburn[5,12], Daniel Gruen[5], Tanishk Mohan[1], Brendan O'Connor[13], Antonella Palmese[13], D. K. Sahu[9], Aditya Pawan Saikia[1], Nikhil Sarin[14,15], Gokul Srinivasaragavan[16,17,18], and Hitesh Tanenia[1]

[1] Department of Physics, Indian Institute of Technology Bombay, Powai, Mumbai 400076, India
[2] Cahill Center for Astrophysics, California Institute of Technology, MC 249-17, 1216 E. California Boulevard, Pasadena, CA 91125, USA
[3] School of Physics and Astronomy, Tel Aviv University, Tel Aviv 6997801, Israel
[4] McWilliams Center for Cosmology and Astrophysics, Department of Physics, Carnegie Mellon University, 5000 Forbes Avenue, Pittsburgh, PA 15213, USA
[5] University Observatory, Faculty of Physics, Ludwig-Maximilians-Universität München, Scheinerstrasse 1, 81679 Munich, Germany
[6] Kavli Institute for Particle Astrophysics and Cosmology, Stanford University, 452 Lomita Mall, Stanford, CA 94305, USA
[7] Department of Astronomy, University of California, Berkeley, CA 94720-3411, USA
[8] Department of Physics and Astronomy, University of North Carolina at Chapel Hill, Chapel Hill, NC 27599, USA
[9] Indian Institute of Astrophysics, II Block Koramangala, Bengaluru 560034, India
[10] Department of Physics and Astronomy, University of North Carolina at Chapel Hill, Chapel Hill, NC 27599-3255, USA
[11] School of Physics and Astronomy, University of Minnesota, Minneapolis, MN 55455, USA
[12] Excellence Cluster ORIGINS, Boltzmannstrasse 2, 85748 Garching, Germany
[13] McWilliams Center for Cosmology and Astrophysics, Department of Physics, Carnegie Mellon University, Pittsburgh, PA 15213, USA
[14] Kavli Institute for Cosmology, University of Cambridge, Madingley Road, CB3 0HA, UK
[15] Institute of Astronomy, University of Cambridge, Madingley Road, CB3 0HA, UK
[16] Department of Astronomy, University of Maryland, College Park, MD 20742, USA
[17] Joint Space-Science Institute, University of Maryland, College Park, MD 20742, USA
[18] Astrophysics Science Division, NASA Goddard Space Flight Center, 8800 Greenbelt Road, Greenbelt, MD 20771, USA
Received 2025 September 2; revised 2025 November 21; accepted 2025 December 8; published 2026 January 8

Abstract

We present a detailed multiwavelength afterglow study of the short gamma-ray burst (GRB) GRB 250704B, extensively monitored in optical and near-infrared bands. Its afterglow displays an unusually long duration plateau followed by an achromatic break and a steep decline, deviating from canonical GRB afterglows. While long plateaus are often explained by central engine activity, we find that for GRB 250704B an energy injection model requires unreasonable parameters. The afterglow is better explained by an off-axis power-law structured jet with a narrow core ($\theta_c \approx 0.^{\circ}7$) viewed at a modest angle ($\theta_v \approx 1.^{\circ}9$). A comparison with GRB 170817A shows that both events are consistent with the off-axis structured jet scenario, where the shape of the light curve is governed primarily by the geometry of the jet and the viewing angle rather than the energetics, microphysical parameters, or external density. Our results underscore the importance of incorporating the jet structure in GRB modeling.

Unified Astronomy Thesaurus concepts: Gamma-ray astronomy (628); Astronomical methods (1043); Gamma-ray sources (633); Optical astronomy (1776)

1. Introduction

Gamma-ray bursts (GRBs) are among the most luminous explosions in the Universe, characterized by an intense prompt γ-ray flash followed by a broadband afterglow (P. Mészáros 2006). The current classification of GRBs is based on the duration of their prompt emission. Bursts whose 90% prompt emission is released in $T_{90} < 2$ s are classified as short GRBs, whereas bursts lasting longer than 2 s are considered long GRBs (C. Kouveliotou et al. 1993). Some short GRBs exhibit extended emission (EE) in the γ-ray band after the initial short flash (e.g., P. Mészáros 2002; J. P. Norris & J. T. Bonnell 2006; J. P. Norris et al. 2010). Given the classical definition, short GRBs with EE can have a significantly longer T_{90}. Because EE is also spectrally softer, classification based solely on T_{90} remains debated (T. Ahumada et al. 2021; B. B. Zhang et al. 2021; J. C. Rastinejad et al. 2022; E. Troja et al. 2022; J. Yang et al. 2022; A. J. Levan et al. 2024).

GRB afterglows, produced by the deceleration of relativistic ejecta in the circumburst medium (CBM), are typically modeled as synchrotron emission from a forward shock. Their light curves often follow a power-law decay in time, punctuated by breaks that can arise from changes in the dynamics or geometry of the outflow. A common cause for such breaks is a "jet break," when the relativistic beaming angle exceeds the physical opening angle of the jet, leading to a faster decline in flux (R. Sari et al. 1999; J. Granot & R. Sari 2002; B. O'Connor et al. 2024). While on-axis afterglows display the canonical bright-to-faint behavior, off-axis afterglows rise more slowly and peak later, as the relativistic beaming cone gradually widens into the observer's line of sight; GW170817/GRB 170817A is a prime example of such off-axis geometry (L. Resmi et al. 2018; E. Troja et al. 2019b; G. Ryan et al. 2020; S. Makhathini et al. 2021). By

[19] These authors contributed equally to the manuscript.
[20] LSST-DA Catalyst Postdoctoral Fellow.

modeling afterglow light curves across wavelengths and incorporating parameters such as jet geometry and observer viewing angle, one can disentangle typical, off-axis, and dark afterglow behaviors and explain the presence and timing of breaks in their evolution.

Some GRB afterglows display an early-time plateau phase, where the light curve remains nearly flat before transitioning into the standard power-law decay. In a purely geometric framework, plateaus can occur in off-axis events when the observer's line of sight is just outside the jet core: as the relativistic beaming cone gradually widens, the observed flux increases or stays constant before declining, producing a plateau-like feature. This effect is much more common in X-ray afterglows, where more than half of Swift-detected bursts show plateaus, whereas in the optical they are relatively rare—only a few dozen have been reported (e.g., GRB 120404A, GRB 140903A, GRB 150424A, GRB 231117A; C. Guidorzi et al. 2014; E. Troja et al. 2016; F. Knust et al. 2017; G. Schroeder et al. 2025a). Other explanations for plateaus, such as sustained central engine activity from a magnetar or late-time energy injection into the blast wave, have been proposed (B. Zhang & P. Mészáros 2001; B. D. Metzger et al. 2008; A. Rowlinson et al. 2013).

Population studies increasingly favor angularly structured jets over simple top-hat jets for both long and short GRBs: modeling shows that a narrow core ($\approx 3^\circ$–5°) with shallower wings can reproduce observed afterglow diversity, luminosity functions, and event rates. The clearest case is GRB 170817A/GW170817, where late-time radio/X-ray evolution and very long baseline interferometry (VLBI) superluminal motion require a successful, narrowly collimated core embedded in wider-angle ejecta (K. P. Mooley et al. 2018, 2022). Beyond GRB 170817A, several bursts show afterglow behavior best explained with structure or modest off-axis viewing, including GRB 140903A and GRB 150101B (a GRB 170817A–like analog at cosmological distance), GRB 160821B (afterglow +kilonova modeling probes jet geometry), and, among long GRBs, the extreme GRB 221009A, whose broadband afterglow prefers a shallow structured jet (E. Troja et al. 2016, 2018; G. P. Lamb et al. 2019; E. Troja et al. 2019a; V. A. Acciari et al. 2021; D. A. Kann et al. 2023; G. P. Srinivasaragavan et al. 2023; B. O'Connor et al. 2023). Recent catalog-level analyses of short GRBs further use afterglow light-curve shapes and viewing angle constraints to argue that structured jets may be common rather than exceptional.

The short GRB 250704B displayed an unusual afterglow: a 1-day plateau followed by a sharp achromatic break and rapid decay, distinguishing it from the known short GRB population. We present results from extensive multiwavelength follow-up and broadband modeling. In Section 2, we describe our observations and data reduction, covering X-ray to radio bands, and list the publicly available datasets used in this work. In Section 3, we briefly summarize the prompt properties of this GRB, based on public data; detailed prompt emission analysis is beyond the scope of this Letter. Section 4 discusses the temporal and spectral behavior of the afterglow. In Section 5, we present broadband modeling of the afterglow. Finally, in Section 6, we summarize our results and compare this GRB with the GW170817 counterpart.

2. Observations and Data

GRB 250704B was first reported by the Space Variable Objects Monitor–Gamma Ray burst Monitor (SVOM-GRM) with trigger time T_0 = 2025-07-04T08:16:27 UT (SVOM/GRM Team et al. 2025). The prompt emission shows a short burst consisting of two episodes with $T_{90} = 0.68 \pm 0.15$ s in the 15–5000 keV band. Several other instruments also reported this burst, including the Einstein Probe–Wide Field Telescope (EP-WXT; A. Li et al. 2025), Konus-Wind (D. Frederiks et al. 2025), the Insight–Hard X-ray Modulation Telescope (HXMT; C.-W. Wang et al. 2025), and the CALET–Gamma-Ray Burst Monitor (Y. Shimizu et al. 2025). The Inter-Planetary Network also reported the detection and triangulation of this burst (A. S. Kozyrev et al. 2025).

An optical counterpart of GRB 250704B was first reported by the COLIBRI at position R.A. (J2000) = $20^{\rm h}03^{\rm m}29\overset{\rm s}{.}51$ and decl. (J2000) = $13^\circ01'23\overset{''}{.}46$, with an uncertainty of $0\overset{''}{.}5$ (B. Schneider et al. 2025). Independent Very Large Telescope (VLT)/FORS2 observations obtained a redshift of 0.661 (D. B. Malesani et al. 2025), which we utilize throughout this Letter. For broadband follow-up observations, we triggered a number of telescopes: GROWTH-India Telescope (GIT), Himalayan Chandra Telescope (HCT), W. M. Keck Telescope (Keck), Victor M. Blanco Telescope (Blanco), Fraunhofer Telescope at Wendelstein Observatory (FTW), Southern Astrophysical Research Telescope, Palomar 200-inch telescope, Palomar 60-inch telescope, and Giant Metrewave Radio Telescope (GMRT), as part of the GROWTH Collaboration (M. M. Kasliwal et al. 2019). We also used data from various circulars reported on the General Coordinate Network (GCN). All data and their sources are listed in Table A1. The observations and data reduction are described in Appendix A.

3. Prompt Emission: Analysis

The prompt emission of the short GRB GRB 250704B was detected by multiple satellites. In this work, we adopt the results reported by Konus-Wind (D. Frederiks et al. 2025). The observed light curve consists of two distinct episodes, which can be interpreted as phases of central engine activity separated by a brief quiescent interval of $\sim$0.1 s. Each episode contains multiple distinct pulses, and the total burst duration is $T_{90} \approx 0.4$s. They report a measured total fluence of $(4.24 \pm 0.65) \times 10^{-6}\,{\rm erg\,cm^{-2}}$ in the 20 keV–10 MeV energy range. The 16 ms peak flux, measured from $T_0 + 0.240$ s, is $(5.82 \pm 0.89) \times 10^{-5}\,{\rm erg\,cm^{-2}\,s^{-1}}$. The time-integrated spectrum from T_0 to $T_0 + 0.256$ s is best fit with a Band function in the 20 keV–15 MeV range, with parameters $\alpha = -1.17^{+0.9}_{-0.8}$, $\beta = -2.48^{+0.39}_{-1.91}$, and an observed peak energy of $E_{p,\rm obs} = 935^{+305}_{-197}$ keV.

Using a redshift of $z = 0.661$, they calculated the isotropic equivalent energy of the burst to be $E_{\rm iso} = (5.15 \pm 0.79) \times 10^{51}$ erg, and the rest-frame peak energy is $E_p = 1550^{+510}_{-330}$ keV. Overall, GRB 250704B exhibits a hard spectrum, consistent with the typical characteristics of short GRBs in their prompt emission.

EP-WXT detected the transient in the soft energy range of 0.5–4 keV, starting at the same T_0 and lasting for 10 s before the observation was interrupted by the autonomous follow-up observation (A. Li et al. 2025). According to the EP-WXT report, the averaged unabsorbed flux is $(1.3 \pm 0.95) \times 10^{-9}\,{\rm erg\,cm^{-2}\,s^{-1}}$ and the corresponding photon index is 1.7 ± 1.3 over the pulse of 10 s. We note that since the observation was terminated by the slew, we cannot comment on whether this might be an extended tail of the prompt emission or the detection of the early afterglow.

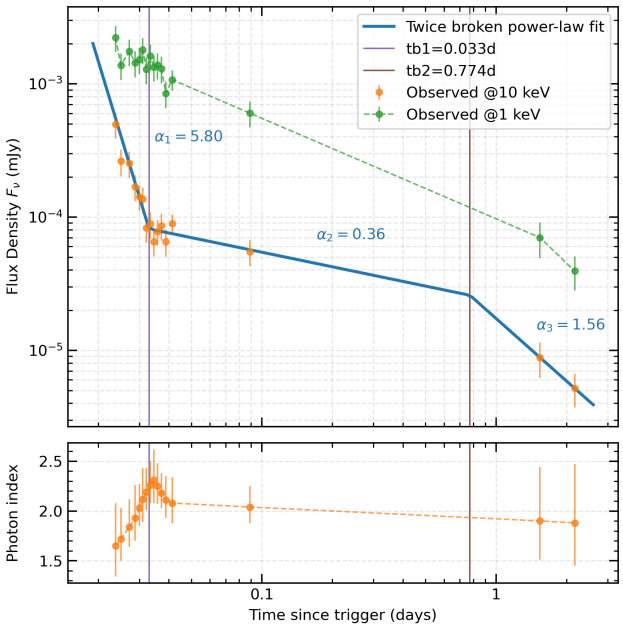

Figure 1. The top panel shows flux densities calculated at 1 keV (green) and 10 keV (orange). The 10 keV light curve is fit with a twice-broken power-law fit (blue). The two temporal breaks are identified at $t_{b1} = 0.033$ days (purple vertical line) and $t_{b2} = 0.774$ days (brown vertical line), with decay indices $\alpha_1 = 5.8$, $\alpha_2 = 0.36$, and $\alpha_3 = 1.56$ marked along the fit. The bottom panel shows the evolution of the photon index. Prior to the first break, the 10 keV flux density exhibits an excess emission with rapid decay, while the 1 keV flux density remains nearly flat.

4. Afterglow

The interaction of the GRB jet with the CBM produces synchrotron radiation, observed as a multiwavelength afterglow that probes the burst energetics and environment (R. Sari 1997; J. Granot & R. Sari 2002). In the simplest framework, the afterglow emission can be described by simple power-law dependencies in both time and frequency, expressed as $F_\nu \propto t^{-\alpha}\nu^{-\beta}$. All afterglow data used in this work are given in Tables A1, A2, and A3.

4.1. X-Ray Afterglow

Figure 1 shows the Swift X-Ray Telescope (XRT) light curve at 10 and 1 keV. The 10 keV flux density exhibits steep initial decay, followed by a much shallower decline. A broken power-law fit yields an initial slope of $\alpha_{X1} = 5.8$, a post-break slope of $\alpha_{X2} = 0.36$, and a break time of $t_{b,X} = 0.03$ days. In contrast, the 1 keV flux density does not show such a rapid decay. This difference arises from spectral evolution: as the spectrum evolves from hard to soft, the 10 keV flux density decays more steeply in the early phases. To avoid contamination from this component, we exclude XRT data prior to $t_{b,X}$ from subsequent analysis.

4.2. Temporal Evolution

We first fit a simple model to the afterglow data to ascertain its basic properties. Our multiwavelength dataset spans X-ray to radio bands. The dataset is particularly rich in the optical r, i, and the infrared J bands. For X-ray analysis, we use 10 keV data from Swift-XRT as discussed in Section 4.1.

GRB 250704B has a galactic latitude of $-10.^\circ04$; hence, galactic extinction ($A_r = 0.3$) cannot be ignored. We corrected optical data for galactic extinction using E. F. Schlafly & D. P. Finkbeiner (2011), while J-band data were corrected using D. J. Schlegel et al. (1998). Note that the unabsorbed X-ray fluxes are calculated using the best-fit N_H values rather than just the galactic ones. The combined light curve exhibits an extended plateau lasting ∼1 day, followed by a rapid decay. We modeled it using a smooth broken power law:

$$F(x) = A\left(\frac{t}{t_b}\right)^{-\alpha_1}\left[\frac{1}{2}\left(1+\left(\frac{t}{t_b}\right)^{1/\delta}\right)\right]^{(\alpha_1-\alpha_2)\,\delta}, \quad (1)$$

where A is the normalization, t_b is the break time, α_1 and α_2 are the temporal decay indices before and after the break, respectively, and δ controls the smoothness of the transition (Astropy Collaboration et al. 2013). Note that the X-ray fit discussed in Section 4.1 does not have this smoothing parameter. We assume an achromatic break to perform a joint fit to the r, i, and J data to obtain $\alpha_1 = -0.13 \pm 0.01$, $\alpha_2 = 3.28 \pm 0.18$, $t_b = 0.96 \pm 0.02$ days, and $\delta = 0.06 \pm 0.05$, confirming a plateau followed by a steep decay. We then scale this achromatic power law to the other bands and show all results in Figure 2. We find that the optical trend is reasonably followed in the X-ray band too—however, our late-time J-band data point is inconsistent with this simplistic model. The achromatic nature of the break suggests that we may be seeing the evolution of a structured jet, or a jet break, though the latter is typically not preceded by a plateau (W. Zhang & A. MacFadyen 2009). No additional breaks are seen in our light curve up to ∼1.67 days.

4.3. Spectral Properties

Assuming a power-law spectrum $F_\nu \propto \nu^{-\beta}$, we now estimate β at various points in the light curve. Our observations are not uniformly spaced, leaving some regions where we have coverage only in a certain band, or some spans with no coverage. Thus, we cannot directly measure the spectral slope at all points. Instead, we estimate fluxes in various bands from our broken power-law fit (Section 4.2) and use it to measure β. Since we have assumed the afterglow evolution including the break to be achromatic, we get $\beta_{o1} = 0.43 \pm 0.06$. Using contemporaneous observations after the break at $(1.2-1.4) \times 10^5$ s, we obtain $\beta_{o2} = 0.66 \pm 0.08$ (Figure 2).

Extending this approach to include X-rays, we calculated the optical-to-X-ray spectral index, giving $\beta_{ox} = 0.73 \pm 0.02$. In the radio regime, detections were obtained at 6 and 10 GHz at about $T_0 + 4$ days separated by just 2.88 hr. We ignore the small time separation and use these values to obtain $\beta_{radio} = 0.96 \pm 0.16$, inconsistent with the optical and X-ray values. Overall, GRB 250704B has a positive β in the light curve in all observed bands.

5. Afterglow Modeling

In the standard fireball model of GRBs, the afterglow originates from synchrotron radiation produced when an ultrarelativistic jet interacts with the CSM (M. J. Rees & P. Meszaros 1992; P. Mészáros & M. J. Rees 1997; R. Sari et al. 1998; J. Granot & R. Sari 2002). The observed temporal and spectral evolution is sensitive to both the physical properties of the jet and the nature of the surrounding medium. By modeling this emission, one can infer key macrophysical

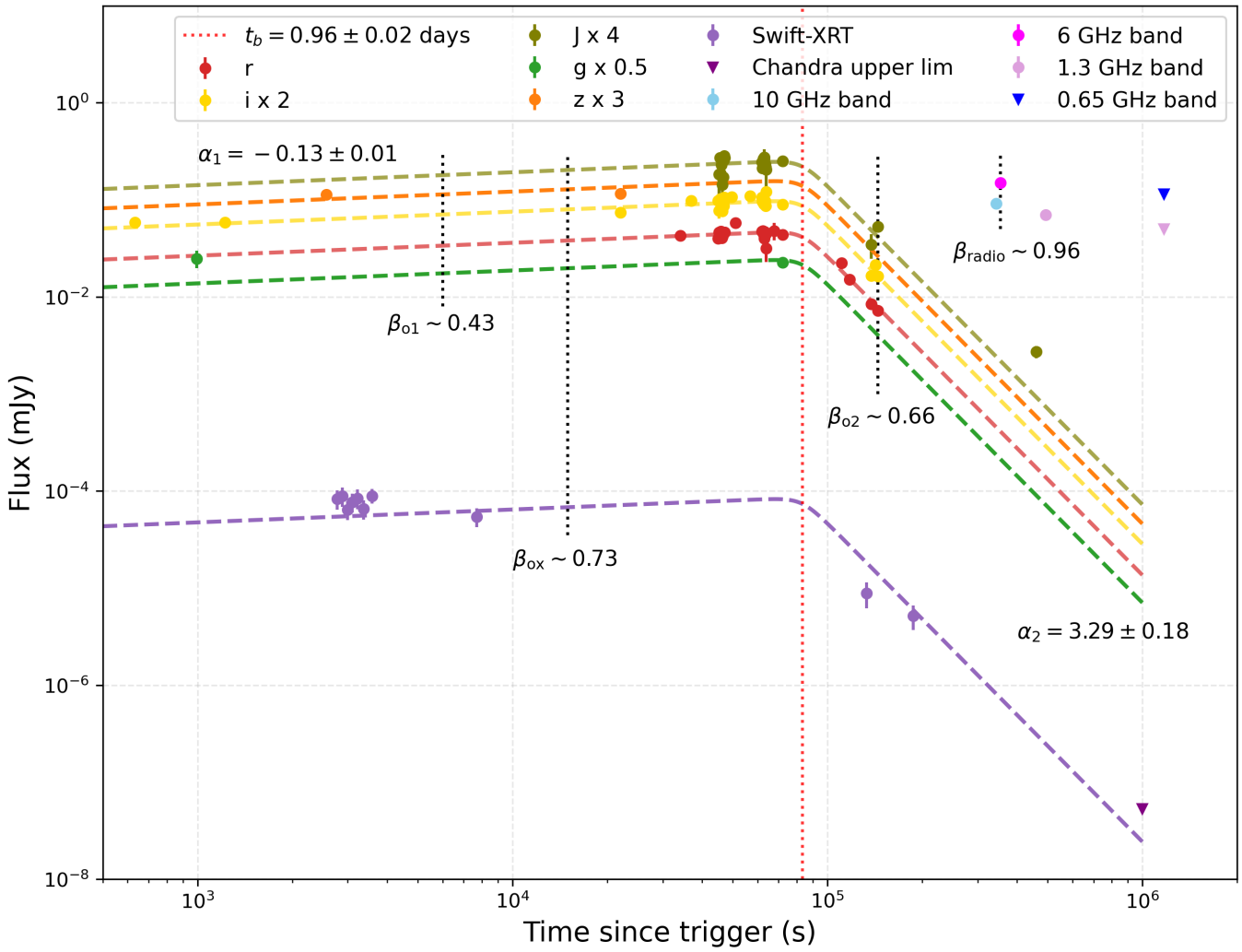

Figure 2. Multiwavelength afterglow light curves of GRB 250704B in X-ray (purple), optical (r, i, z, g, and J bands), and radio (1.3, 6, and 10 GHz, with an upper limit at 0.65 GHz). The light curves are well described by a broken power law with an initial shallow plateau phase ($\alpha_1 = -0.13 \pm 0.01$) followed by a steep decay ($\alpha_2 = 3.29 \pm 0.18$) after the break at $t_b = 0.96 \pm 0.02$ days (red vertical line). Spectral indices from the fits are $\beta_{o1} = 0.43 \pm 0.06$ (optical) and $\beta_{ox} = 0.73 \pm 0.02$ (optical-to-X-ray), while those derived from observations are $\beta_{o2} = 0.66 \pm 0.08$ (optical) and $\beta_{radio} = 0.96 \pm 0.16$ (radio). The consistent temporal evolution across X-ray, optical, and radio bands indicates an achromatic break, supporting an off-axis jet interpretation.

parameters such as the isotropic equivalent kinetic energy ($E_{K,iso}$), jet opening angle (θ_c), and observer viewing angle (θ_v), as well as microphysical parameters such as the electron power-law index (p), the fraction of energy in relativistic electrons (ϵ_e) and magnetic fields (ϵ_b), and the fraction of accelerated particles (χ). In this work, we assume $\chi = 1$, such that all accelerated electrons contribute to nonthermal synchrotron emission. The temporal and spectral evolution of the afterglow depends on the synchrotron break frequencies: the characteristic frequency (ν_m), the cooling frequency (ν_c), and the self-absorption frequency (ν_a; R. Sari 1997; J. Granot & R. Sari 2002). In addition, the viewing angle relative to the jet axis can strongly influence the observed light curve (J. Granot et al. 2002; N. Fraija et al. 2022).

In this Letter we explore an afterglow viewed off-axis with a structured jet, as it is the model that better describes the physics of this GRB. Our modeling for an on-axis jet with additional energy injection can be found in Appendix C.

5.1. Data Selection

For afterglow modeling, we used all available optical data and the Swift-XRT flux density at 10 keV. As discussed in Section 4.1, we ignore initial XRT data. For both optical and X-ray data, synchrotron self-absorption is negligible because it affects only radio frequencies.

However, in the radio band, self-absorption plays a significant role at low frequencies. Thus, the flux evolution of the radio band depends not only on the cooling (ν_c) and characteristic (ν_m) frequencies but also on the absorption frequency (ν_a). For short GRBs, the circumburst environment is usually a uniform low-density interstellar medium (ISM; W. Fong et al. 2015; B. O'Connor et al. 2020). In this case, ν_a depends primarily on the ISM density (n_0) and remains constant during the afterglow. Low frequencies ($\sim$GHz) are often impacted by self-absorption, while higher frequencies like 6 and 10 GHz are typically unaffected. Hence, we exclude the 1.3 GHz data from our modeling.

5.2. Numerical Modeling Using jetsimpy

We modeled the multiwavelength afterglow using the publicly available package jetsimpy (H. Wang et al. 2024), which calculates the synchrotron emission from a structured relativistic jet interacting with an external medium. Unlike the point-source approximation (D. Eichler & A. Levinson 2004; J. Granot et al. 2018; N. Fraija et al. 2023), jetsimpy computes the observed flux by integrating over the entire jet surface, taking into account relativistic beaming, angular structure of the jet, and light travel time effects. The code employs a reduced hydrodynamic model that represents the blast wave as an infinitely thin, 2D surface. By assuming an axially symmetric jet, the simulation reduces into a 1D problem, enabling efficient computation of the jet's angular evolution and lateral spreading at late times.

We assumed a power-law jet defined as

$$E(\theta) = E_{K,\rm iso}\left[1+\left(\frac{\theta}{\theta_c}\right)^2\right]^{-s/2}, \quad (2)$$

$$\Gamma_j(\theta) = (\Gamma_0 - 1)\left[1+\left(\frac{\theta}{\theta_c}\right)^2\right]^{-s/2} + 1, \quad (3)$$

where $E_{K,\rm iso}$ is the isotropic equivalent energy, $\Gamma_{j,0}$ is the initial Lorentz factor, θ_c is the half-opening angle of the jet, and s is the power-law index (H. Wang et al. 2024). In our fits, we adopt a nominal value of $s = 6$ (G. Ryan et al. 2024) and allow the jet to spread. The model does not incorporate synchrotron self-absorption.

We initially allowed $\Gamma_{j,0}$ to vary as a free parameter, but the sampler consistently converged to very large values (>1000). In contrast, fixing $\Gamma_{j,0}$ to a low value forced the model to compensate by requiring a very dense CBM, inconsistent with typical short GRB environments. Therefore, in our modeling we have fixed $\Gamma_{j,0}$ to be sufficiently high (10^{100}) that the blast wave begins directly in the deceleration phase, without an appreciable coasting stage. Note that jets with high Lorentz factor (>1000) have been seen in short GRBs, for example, GRB 090510 (M. Ackermann et al. 2010; H.-N. He et al. 2011; N. Fraija et al. 2016).

We initially allowed $\Gamma_{j,0}$ to vary as a free parameter, but the sampler consistently converged to very large values (>1000). In contrast, fixing $\Gamma_{j,0}$ to a low value forced the model to compensate by requiring a very dense CBM, inconsistent with typical short GRB environments. Therefore, in our modeling, we assumed the absence of a coasting phase and presume an arbitrarily large initial Lorentz factor (by setting $\Gamma_{j,0} \sim 10^{100}$) so that the blast wave begins directly in the deceleration phase (H. Wang et al. 2024).

High Lorentz factors ($\Gamma_{j,0} \gtrsim 10^3$) have been inferred in some short GRBs, such as GRB 090510, which was detected by Fermi-LAT and showed bright high-energy emission (M. Ackermann et al. 2010; H.-N. He et al. 2011; N. Fraija et al. 2016). Similar high values of $\Gamma_{j,0}$ have been discussed in the context of Fermi-LAT–detected bursts by various authors (R. Hascoët et al. 2012; N. Fraija et al. 2024). For completeness, we retrieved the Fermi Gamma-ray Burst Monitor daily data from the Fermi Science Support Center archive[21] and processed them using GDT-Fermi (A. Goldstein et al. 2023). We found that at the trigger time of GRB 250704B Fermi was offline owing to its position in the South Atlantic Anomaly and therefore did not observe the burst with any of its instruments, including Fermi-LAT. Thus, the lack of LAT detection does not contradict the large $\Gamma_{j,0}$ inferred from our modeling, which remains physically plausible.

[21] https://fermi.gsfc.nasa.gov/ssc/data/access/

Table 1
Summary of the Priors and Posteriors for the Model Parameters Obtained from MultiNest Fitting for Off-axis Structured Jet Model

Parameter	Unit	Prior Type	Parameter Bound	Posterior Value
$\log_{10}(E_{K,\rm iso})$	erg	uniform	[51, 56]	54.17 ± 0.12
$\log_{10}(\epsilon_b)$	⋯	uniform	[−5, −1]	-2.06 ± 0.48
$\log_{10}(\epsilon_e)$	⋯	uniform	[−3, −0.5]	$-0.64^{+0.10}_{-0.15}$
$\log_{10}(n_0)$	$\rm cm^{-3}$	uniform	[−4, 1]	-1.86 ± 0.75
θ_c	rad	log-uniform	$[10^{-4}, 0.2]$	0.012 ± 0.003
θ_v	rad	log-uniform	$[10^{-4}, 0.2]$	0.032 ± 0.008
p	⋯	uniform	[2.001, 2.8]	2.04 ± 0.01
χ	⋯	fixed	1	1

Note. The posterior values are presented with their uncertainties, and parameter bounds are listed separately for clarity where applicable.

We then constrained the model parameters ($E_{K,\rm iso}$, ϵ_b, ϵ_e, n_0, θ_c, θ_v, and p) using the Nested Sampling library MultiNest, implemented via PyMultiNest (J. Buchner et al. 2014), with 2000 live points. The priors and best-fit values are listed in Table 1, with posterior distributions in Figure B1 in Appendix B. The best-fit model (Figure 3(a)) reproduces both the plateau and the sharp decay, with the achromatic break across all bands indicating a geometric jet break from an off-axis structured jet. Observed flux densities are shown as circles, median model light curves as dashed lines, and 3σ uncertainties as shaded bands. The Swift-XRT data at the earliest epochs, $t < t_{b,\rm X}$ (see Section 4.1), are shown as hollow markers for both the 1 and 10 keV light curves. Note that these early data were excluded from the fitting procedure. The 1 keV XRT data are consistent with the best-fit model, whereas the 10 keV data deviate significantly at early time. This steep initial decline can be attributed to a hard-to-soft spectral evolution due to high-latitude emission (HLE), a behavior previously observed in multiple GRBs such as GRB 061121, GRB 060607A, and GRB 100906A (S. Ascenzi et al. 2020; G. Oganesyan et al. 2020; A. Panaitescu 2020). HLE has been reported in both on-axis and off-axis scenarios, although in the latter case the transition from the steep decay to the plateau phase could be smoother, depending on the jet structure and observer's viewing angle.

The posterior distributions for GRB 250704B indicate a highly energetic jet with $E_{K,\rm iso} = (1.5 \pm 1.4) \times 10^{54}$erg, consistent with the long-lived plateau observed for GRB 250704B. The CBM density is constrained to $n_0 = 0.01$ $\rm cm^{-3}$, consistent with expectations for short GRBs (W. Fong et al. 2015; B. O'Connor et al. 2020). The microphysical parameters are $\epsilon_e = 0.23^{+0.05}_{-0.07}$, $\epsilon_b = 0.008^{+0.016}_{-0.006}$, and $p = 2.04 \pm 0.02$. For the structured jet, we obtain a narrow core angle of $\theta_c \approx 0.69°$ and a viewing angle of $\theta_v \approx 1.^{\circ}83$. This implies that 75% of the total energy is concentrated within the narrow jet ($\simeq\theta_c$), and it declines at higher viewing angles. Within the obtained θ_v, the fraction of total energy within the jet is 98.5%.

Figure 3(b) shows the spectral energy distributions (SEDs) from the off-axis structured jet model at $t = 0.17$ days,

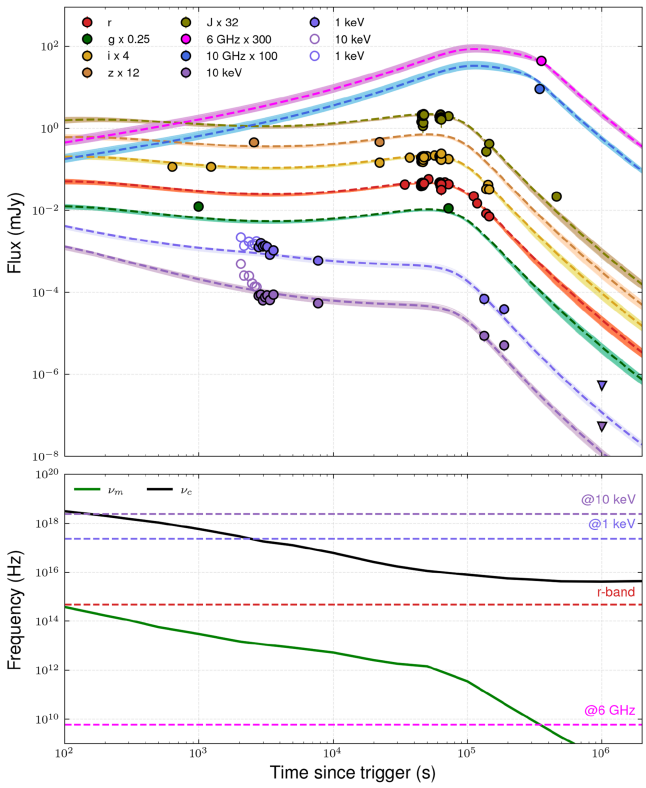

Figure 3. Afterglow modeling of GRB 250704B using `jetsimpy` modeled with a power-law structured jet propagating into a uniform ISM viewed slightly off-axis. (a) Top panel: multiband afterglow light curves with dotted lines show the best-fit light curves, and shaded regions mark the 3σ uncertainties. Open symbols denote data points excluded from the fit. Bottom panel: synchrotron break frequencies ν_m and ν_c as a function of time, calculated from the model. (b) SEDs at multiple epochs, 0.17 days (purple), $t = 0.96$ days (green), $t = 1.53$ days (red), and $t = 4.04$ days (yellow), with corresponding derived spectrum from temporal-fit, observed optical–X-ray, and radio data.

$t = 0.96$ days, $t = 1.53$ days, and $t = 4.04$ days. At $t = 0.17$ days, we include the temporally extrapolated spectrum from the light-curve fit, while at later epochs the observed optical data are shown at $t = 1.53$ days and radio measurements are shown at $t = 4.04$ days. Across all epochs, the optical SEDs follow a consistent spectral slope β, demonstrating achromatic evolution in this regime. This agreement between the model and the sparse multiwavelength data highlights the robustness of the structured jet interpretation.

Next, we examine the evolution of the synchrotron break frequencies, ν_c and ν_m, during the observed light curve. Since the jet is being observed significantly off-axis, we cannot use simple analytic estimates for the evolution of these frequencies with time. Instead, we derive the temporal behavior of these frequencies from the best-fit model at different epochs. As seen in the bottom panel of Figure 3(a), we find that the cooling frequency, ν_c, remains above all the observed bands throughout the duration of the observations. The characteristic frequency, ν_m, crosses the optical band at very early times, before observations commence, and subsequently passes through the radio band at ∼4 days after the GRB trigger.

Based on the evolution of the synchrotron break frequencies, most of the optical afterglow is observed in the adiabatic cooling regime ($\nu_m < \nu_{\rm optical} < \nu_c$) barring a few early data points. In this regime, the closure relation for a jet expanding into a uniform ISM predicts a spectral slope of $\beta = (p-1)/2 = 0.52 \pm 0.01$, which is comparable to the measured spectral indices ($\beta_{\rm o1}$, $\beta_{\rm o2}$) derived in Section 4.3. In contrast, the radio band lies in the $\nu_{\rm radio} < \nu_m$ regime, where a positive spectrum with $F_\nu \propto \nu^{1/3}$ is expected. However, the spectral index $\beta_{\rm radio}$ derived in Section 4.3 shows a negative slope: inconsistent with standard synchrotron theory, but consistent with jet break from an off-axis structured jet. Furthermore, the temporal decay index (α) does not solely follow the standard closure relations of synchrotron emission but is also modulated by the viewing geometry of an off-axis structured jet.

The radiative efficiency of a GRB quantifies the fraction of the total energy budget emitted as prompt γ-rays (N. M. Lloyd-Ronning & B. Zhang 2004). If we directly calculate this value for GRB 250704B, we get a very low number: $\eta \sim 0.3\%$, rather than the expected 10%–20% range expected for the fireball model with internal shocks (P. Kumar 1999; A. Maxham & B. Zhang 2009; X.-G. Wang et al. 2015). The reason for this apparent discrepancy is that the efficiency definition is to be applied for an on-axis observer, where the observed emission is dominated by material along the line of sight. This shows the importance of ascertaining whether the observer is within the jet core before interpreting the apparent jet efficiencies. To consistently compare the jet kinetic energy during the afterglow phase ($E_{K,\rm iso}$) with the prompt emission in the efficiency calculation, the observed (line-of-sight) prompt energy $E_{\rm iso}$ must be corrected to its on-axis (core) value. In this case, the Doppler factor does not play a role (B. O'Connor et al. 2024), and the prompt γ-ray energy can be approximated from the jet's angular energy profile (Equation (2)), assuming no angular dependence of the γ-ray efficiency.

6. Discussion

6.1. Structure of the Jet

The light curve of GRB 250704B shows several distinctive features compared to typical GRBs: (1) a pronounced long plateau in the optical light curve from the first detection at 10.5 minutes to the break time, $t_b = 0.96 \pm 0.02$ days; (2) a steep post-break decay with $\alpha = 3.29 \pm 0.18$; (3) an achromatic break in both X-ray and optical bands; and (4) negative spectral decay indices (β) before and after the break across all bands.

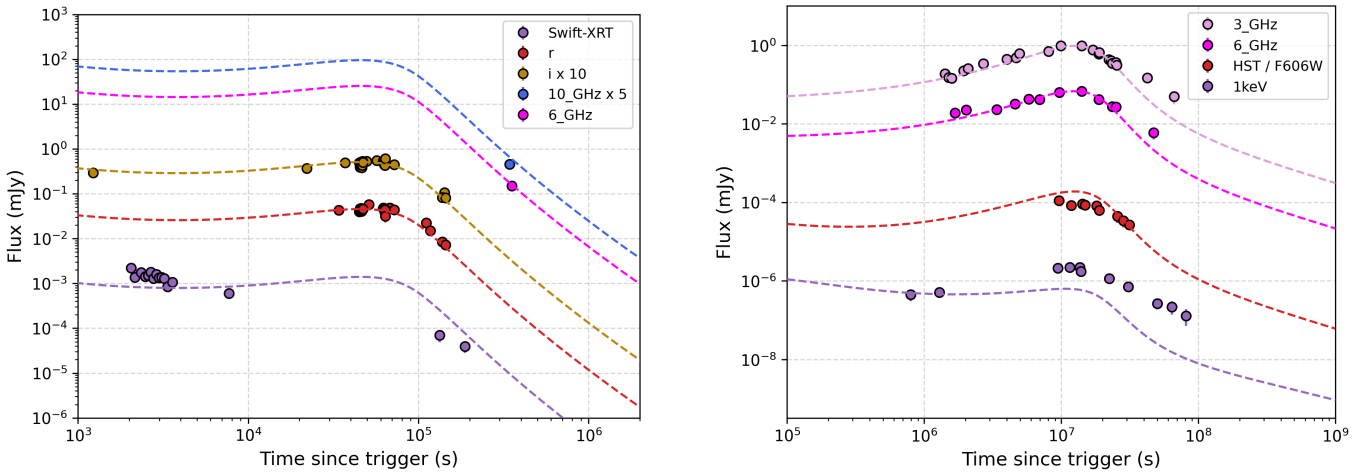

(a) Model originally fit to GW170817 (G. Ryan et al. 2024) but recomputed using the core angle and viewing-angle ratio inferred for GRB 250704B ($\theta_v - \theta_c \approx 1.1°$, $\theta_v/\theta_c \approx 2.7$). The modeled flux is scaled up to match observed afterglow of GRB 250704B.

(b) Model from our fit to GRB 250704B recomputed using the core angle and viewing-angle ratio inferred for GW170817 ($\theta_v - \theta_c \approx 14°$, $\theta_v/\theta_c \approx 4.5$). The afterglow data of GW170817 event is collected from (S. Makhathini et al. 2021).

Figure 4. Comparison of structured jet geometries between GRB 250704B and the GW170817 afterglow. (a) Model originally fit to GW170817 (G. Ryan et al. 2024) but recomputed using the core angle and viewing angle ratio inferred for GRB 250704B ($\theta_v - \theta_c \approx 1.^\circ1$, $\theta_v/\theta_c \approx 2.7$). The modeled flux is scaled up to match the observed afterglow of GRB 250704B. (b) Model from our fit to GRB 250704B recomputed using the core angle and viewing angle ratio inferred for GW170817 ($\theta_v - \theta_c \approx 14°$, $\theta_v/\theta_c \approx 4.5$). The afterglow data of the GW170817 event are collected from S. Makhathini et al. (2021).

A nominal model consisting of a top-hat jet expanding into an ISM environment cannot create long plateaus. In most cases, the light curves show a rise, a peak, and a decline. An observer located just beyond the jet core at, say, $\theta_v/\theta_c = 1.1$ may observe short plateaus (see, e.g., A. Panaitescu & W. T. Vestrand 2008), but extending the duration to $\sim 10^5$ s would make the plateau unrealistically bright. Top-hat jet afterglows do show achromatic jet breaks, but these typically occur after a relatively shallow decay phase. In contrast, the light curve of GRB 250704B exhibits a plateau followed by a very steep decline, which is inconsistent with the jet break scenario.

On the other hand, a power-law structured jet observed off-axis can naturally produce both a late-time peak and a long-lasting plateau (A. Panaitescu & W. T. Vestrand 2008). For a general structured jet, the isotropic equivalent energy of the blast wave depends on the angle from the jet axis, expressed as $E(\theta) = 4\pi dE/d\Omega$. The launch mechanism initially sets the angular structure of the jet and can subsequently be modified by interaction with the external medium. In the case of short GRBs associated with compact object mergers, the ejecta along the polar direction is relatively sparse. Hence, the jet structure remains largely unchanged from its original form (G. Ryan et al. 2020).

For an off-axis structured jet model, the early rise and plateau phases are highly sensitive to the jet structure and can be used to infer jet geometry (G. Ryan et al. 2024; E. Nakar & T. Piran 2021). In contrast, the post-peak declining phase of the light curve provides limited constraints on the jet geometry, since it closely resembles the evolution of an on-axis afterglow. Moreover, the ratio θ_v/θ_c modulates the morphology of the light curve before peak. If this ratio is close to unity, the light curve shows a decay; for larger ratios, a rising behavior is observed. The peak in the light curve is determined by both the jet's core angle and the viewing-to-core angle ratio. For GRB 250704B, we infer a narrow jet with $\theta_c \sim 0.^\circ7$ and an intermediate ratio of $\theta_v/\theta_c \approx 2.73$, which naturally explains the observed long plateau followed by a steeper decay, consistent with an early-peaking light curve.

6.2. Comparison with GW170817

The GRB afterglow of the GW170817 had, in addition to a detailed light curve (S. Makhathini et al. 2021, and references therein), a VLBI measurement of its image at superluminal motion across the sky (K. P. Mooley et al. 2018; G. Ghirlanda et al. 2019; K. P. Mooley et al. 2022). The image motion confirmed that the afterglow is generated by an off-axis jet and enabled a tight measurement of the viewing angle, $\theta_v \approx 19°$ with an estimated error of a few degrees, and jet core angle ($\theta_c \approx 1.^\circ5 - 4°$) at the time of the peak, about 150 days after the merger (T. Govreen-Segal & E. Nakar 2023). A detailed numerical modeling of the jet expansion has shown that the initial jet opening angle (before spreading) was in the range $\sim 0.^\circ5$–$4°$ and that the observations are best explained by a power-law structured jet with $s \approx 3$–4 (T. Govreen-Segal & E. Nakar 2024). Due to degeneracies between the model parameters, the density into which the jet propagated is not well constrained, and it was probably around 10^{-3} cm^{-3}, with an uncertainty of at least an order of magnitude (see, e.g., E. Troja et al. 2019b). In addition, the initial jet isotropic equivalent energy in the core is not well constrained, and it most likely was about one or two orders of magnitude lower than the value that we infer for GRB 250704B. In our discussion, we adopt the values of $\theta_c = 4°$ and $\theta_v/\theta_c = 4.5$ for GW170817.

For an off-axis GRB, the time at which the afterglow peaks depends on the viewing geometry and the ratio of the isotropic equivalent kinetic energy to the circumburst density, but it is only weakly sensitive to the core angle (T. Govreen-Segal & E. Nakar 2024). In particular, it is proportional to $(\theta_v - \theta_c)^2$. Since this value is about 14° for GW170817 but only $\sim 1.^\circ1$ for GRB 250704B, the light-curve peak shifts from $\sim$162 days (E. Troja et al. 2019b) to $\sim$1 day.

We undertake a direct comparison between GW170817 and GRB 250704B. First, we take the model parameters of GW170817 from G. Ryan et al. (2024) and change θ_c and θ_v values to those of GRB 250704B. We then apply a scale factor to the model, and resultant curves are shown in Figure 4(a), along with observed data. We see a good agreement in the two. Due to the low value of θ_v–θ_c, the light curve peaks much earlier, while the low value of θ_c causes the early light curve to be a plateau rather than a rise, as discussed in T. Govreen-Segal & E. Nakar (2024). Next, we take model parameters of GRB 250704B but change θ_c to 4° and θ_v to 18°. The resultant light curves, again scaled by an overall factor, are shown in Figure 4(b). Despite other parameters being fit to GRB 250704B data, the model shows reasonable correspondence with observed values for GW170817.

We therefore conclude that both GRB 250704B and GW170817A can be consistently described within the off-axis structured jet framework, with their contrasting light-curve evolution being dominated by differences in jet and viewing geometry. In particular, the narrower jet core and intermediate viewing angle ratio of GRB 250704B explain its earlier peak and extended plateau, while the broader jet and larger ratio of GW170817 result in the much later peak. This comparison highlights the importance of long-term follow-up of short GRBs, since structured jets with larger θ_v–θ_c values may remain undetected until very late times.

Acknowledgments

We thank the anonymous referee for the comments and suggestions that have helped us to improve the Letter.

We thank all members of the GROWTH collaboration for helping with observations and data processing.

GIT (H. Kumar et al. 2022) is a 70 cm telescope with a 0.°7 field of view, set up by the Indian Institute of Astrophysics (IIA) and the Indian Institute of Technology Bombay (IITB) with funding from DST-SERB and IUSSTF. It is located at the Indian Astronomical Observatory (IAO; Hanle), operated by IIA. We acknowledge funding by the IITB alumni batch of 1994, which partially supports the operations of the telescope. Telescope technical details are available at https://sites.google.com/view/growthindia/.

This work is partially based on data obtained with the 2 m HCT of IAO under the proposal 2025-02-P10 (PI: D. Eappachen). We thank the staff of IAO, Hanle, and CREST, Hosakote, who made these observations possible. The facilities at IAO and CREST are operated by the Indian Institute of Astrophysics, Bangalore. We thank the staff of the GMRT who made these observations possible. GMRT is run by the National Centre for Radio Astrophysics of the Tata Institute of Fundamental Research.

Some of the data presented herein were obtained at Keck Observatory, which is a private 501(c)3 nonprofit organization operated as a scientific partnership among the California Institute of Technology, the University of California, and the National Aeronautics and Space Administration. The Observatory was made possible by the generous financial support of the W. M. Keck Foundation. The authors wish to recognize and acknowledge the very significant cultural role and reverence that the summit of Maunakea has always had within the Native Hawaiian community. We are most fortunate to have the opportunity to conduct observations from this mountain.

M.W.C. acknowledges support from the National Science Foundation with grant Nos. PHY-2117997, PHY-2308862, and PHY-2409481.

N.S. is supported by a fellowship from the Kavli Foundation.

A.P. acknowledges support by the National Science Foundation AST grant No. 2308193. This project used data obtained with the Dark Energy Camera (DECam), which was constructed by the Dark Energy Survey (DES) collaboration. Based on observations at Cerro Tololo Inter-American Observatory, NSF's NOIRLab (NOIRLab Prop. ID 2025A-729671, PI: Palmese), which is managed by the Association of Universities for Research in Astronomy (AURA) under a cooperative agreement with the National Science Foundation.

M.K. and V.B. acknowledge the support from the VAIBHAV Fellowship of the Department of Science and Technology of the Government of India.

V.B. and the IIT Bombay team sincerely thank BDP UGL Global Logistics Pvt. Ltd. for their generous CSR support toward our computational needs.

We thank Anirudh Salgundi and Arjun Ghosh for help with the Chandra proposal. We thank Ashwin Devaraj for useful discussions.

G.C.A. thanks the Indian National Science Academy (INSA) for support under their Senior Scientist Programme.

The scientific results reported in this article are based on observations made by the Chandra X-ray Observatory. This research has made use of software provided by the Chandra X-ray Center (CXC) in the application packages CIAO.

S.A. is supported by an LSST-DA Catalyst Fellowship, funded through the support of grant 62192 from the John Templeton Foundation to LSST-DA. S.A. also gratefully acknowledges support from Stanford University, the US Department of Energy, and Fred Kavli and the Kavli Foundation.

The Andreoni Transient Astronomy Lab is supported by the National Science Foundation award AST 2505775, NASA grant 24-ADAP24-0159, and the Discovery Alliance Catalyst Fellowship Mentors award 2025-62192-CM-19.

Funded in part by the Deutsche Forschungsgemeinschaft (DFG, German Research Foundation) under Germany's Excellence Strategy–EXC-2094–390783311.

Facilities: Swift (XRT), Chandra, GIT, HCT, Keck:I, Blanco, WO:2m (FTW), Hale (Palomar 200-inch telescope), PO:1.5 (Palomar 60-inch telescope), GMRT.

Software: Astropy (Astropy Collaboration et al. 2013, 2018; Astropy Collaboration et al. 2022), Source Extractor (E. Bertin & S. Arnouts 1996), Astro-SCRAPPY (C. McCully & M. Tewes 2019), `solve-field` astrometry engine (D. Lang et al. 2010), `PSFEx` (E. Bertin 2013), `jetsimpy` (H. Wang et al. 2024), `ciao-4.15` (A. Fruscione et al. 2006), `afterglowpy` (G. Ryan et al. 2020, 2024), `PyMultiNest` (J. Buchner et al. 2014), `CASA` (Team CASA et al. 2022).

Author Contribution

All authors contributed equally to this collaborative work.

Appendix A
Afterglow Data

In this appendix we list and describe the photometry collected for the analysis of GRB 250704B, along with the reduction and calibration methods. All optical and near-infrared data are presented in Table A1. The X-ray and radio afterglow data are compiled in Tables A2 and A3, respectively.

Table A1
Multiwavelength Afterglow Observations of GRB 250704B from Optical Bands

Time T_0 (s)	Filter	Frequency ($\times 10^{14}$ Hz)	Mag (AB)	Lim Mag (AB)	Corr Mag (AB)	Instrument	References
37044	*i*	3.931700	19.90 ± 0.10	⋯	19.67 ± 0.10	JinShan	X. Liu et al. (2025)
1224	*i*	3.931700	20.46 ± 0.06	⋯	20.23 ± 0.06	COLIBRI	B. Schneider et al. (2025)
2568	*z*	3.282160	20.12 ± 0.05	⋯	19.95 ± 0.05	ESO-VLT-FORS2	D. B. Malesani et al. (2025)
16848	*VT_B*	6.050000	20.40 ± 0.20	⋯	19.92 ± 0.20	SVOM/VT	L. P. Xin et al. (2025)
16848	*VT_R*	3.810000	20.40 ± 0.20	⋯	20.19 ± 0.20	SVOM/VT	L. P. Xin et al. (2025)
22053	*i*	3.931700	20.20 ± 0.03	⋯	19.97 ± 0.03	Pan-STARRS	J. H. Gillanders et al. (2025)
22053	*z*	3.282160	20.01 ± 0.07	⋯	19.84 ± 0.07	Pan-STARRS	J. H. Gillanders et al. (2025)
34101	*r*	4.811310	20.12 ± 0.08	⋯	19.82 ± 0.08	GIT	This work
49648	*i*	3.931700	19.81 ± 0.09	⋯	19.58 ± 0.09	GIT	This work
51115	*r*	4.811310	19.80 ± 0.09	⋯	19.50 ± 0.09	GIT	This work
57708	*i*	3.931700	19.78 ± 0.05	⋯	19.55 ± 0.05	NOT	A. Martin-Carrillo et al. (2025)
63108	*r*	4.811310	20.20 ± 0.10	⋯	19.90 ± 0.10	FTW-3KK	M. Busmann et al. (2025)
63108	*i*	3.931700	19.90 ± 0.10	⋯	19.67 ± 0.10	FTW-3KK	M. Busmann et al. (2025)
63108	*J*	2.400000	19.40 ± 0.20	⋯	19.31 ± 0.20	FTW-3KK	M. Busmann et al. (2025)
67680	*r*	4.811310	20.00 ± 0.20	⋯	19.70 ± 0.20	ESO-VLT-UT3	J. An et al. (2025a)
72000	*g*	6.284960	20.20 ± 0.10	⋯	19.76 ± 0.10	GSP, LCO	W. X. Li et al. (2025)
72000	*r*	4.811310	20.10 ± 0.10	⋯	19.80 ± 0.10	GSP, LCO	W. X. Li et al. (2025)
72000	*i*	3.931700	20.00 ± 0.10	⋯	19.77 ± 0.10	GSP, LCO	W. X. Li et al. (2025)
72000	*J*	2.400000	19.50 ± 0.10	⋯	19.41 ± 0.10	ESO-VLT-UT4-HAWK-I	Y.-H. Yang et al. (2025)
111111	*r*	4.811310	20.83 ± 0.05	⋯	20.53 ± 0.05	GIT	This work
118102	*R*	4.686720	21.06 ± 0.05	⋯	20.77 ± 0.05	AZT-33IK, Mondy	A. Volnova et al. (2025)
142344	*i*	3.931700	21.56 ± 0.14	⋯	21.33 ± 0.14	NOT	J. An et al. (2025b)
460800	*J*	2.400000	24.40 ± 0.20	⋯	24.31 ± 0.20	Keck-MOSFIRE	This work
45258	*r*	4.811310	20.04 ± 0.12	⋯	19.74 ± 0.12	FTW-3KK	This work
45553	*r*	4.811310	20.14 ± 0.07	⋯	19.84 ± 0.07	FTW-3KK	This work
45764	*r*	4.811310	20.04 ± 0.06	⋯	19.74 ± 0.06	FTW-3KK	This work
45976	*r*	4.811310	20.02 ± 0.06	⋯	19.72 ± 0.06	FTW-3KK	This work
46188	*r*	4.811310	20.19 ± 0.08	⋯	19.88 ± 0.08	FTW-3KK	This work
46399	*r*	4.811310	20.15 ± 0.08	⋯	19.85 ± 0.08	FTW-3KK	This work
46611	*r*	4.811310	20.11 ± 0.07	⋯	19.81 ± 0.07	FTW-3KK	This work
46823	*r*	4.811310	20.06 ± 0.06	⋯	19.76 ± 0.06	FTW-3KK	This work
47034	*r*	4.811310	20.03 ± 0.06	⋯	19.73 ± 0.06	FTW-3KK	This work
47246	*r*	4.811310	20.04 ± 0.06	⋯	19.74 ± 0.06	FTW-3KK	This work
61902	*r*	4.811310	20.02 ± 0.03	⋯	19.71 ± 0.03	FTW-3KK	This work
62114	*r*	4.811310	20.03 ± 0.05	⋯	19.72 ± 0.05	FTW-3KK	This work
62326	*r*	4.811310	20.00 ± 0.03	⋯	19.70 ± 0.03	FTW-3KK	This work
62537	*r*	4.811310	20.04 ± 0.04	⋯	19.74 ± 0.04	FTW-3KK	This work
62749	*r*	4.811310	20.11 ± 0.05	⋯	19.80 ± 0.05	FTW-3KK	This work
62961	*r*	4.811310	20.09 ± 0.05	⋯	19.79 ± 0.05	FTW-3KK	This work
63172	*r*	4.811310	20.03 ± 0.06	⋯	19.73 ± 0.06	FTW-3KK	This work
63384	*r*	4.811310	20.09 ± 0.05	⋯	19.79 ± 0.05	FTW-3KK	This work
63596	*r*	4.811310	20.09 ± 0.07	⋯	19.79 ± 0.07	FTW-3KK	This work
63808	*r*	4.811310	20.45 ± 0.27	⋯	20.15 ± 0.27	FTW-3KK	This work
45258	*i*	3.931700	20.15 ± 0.18	⋯	19.93 ± 0.18	FTW-3KK	This work
45553	*i*	3.931700	19.92 ± 0.07	⋯	19.69 ± 0.07	FTW-3KK	This work
45764	*i*	3.931700	19.85 ± 0.07	⋯	19.62 ± 0.07	FTW-3KK	This work
45976	*i*	3.931700	20.08 ± 0.09	⋯	19.86 ± 0.09	FTW-3KK	This work
46188	*i*	3.931700	19.96 ± 0.08	⋯	19.73 ± 0.08	FTW-3KK	This work
46399	*i*	3.931700	20.16 ± 0.10	⋯	19.94 ± 0.10	FTW-3KK	This work
46611	*i*	3.931700	19.90 ± 0.08	⋯	19.68 ± 0.08	FTW-3KK	This work
46823	*i*	3.931700	20.03 ± 0.08	⋯	19.81 ± 0.08	FTW-3KK	This work
47034	*i*	3.931700	19.81 ± 0.06	⋯	19.59 ± 0.06	FTW-3KK	This work
47246	*i*	3.931700	19.87 ± 0.06	⋯	19.65 ± 0.06	FTW-3KK	This work
61902	*i*	3.931700	19.82 ± 0.04	⋯	19.59 ± 0.04	FTW-3KK	This work
62114	*i*	3.931700	19.92 ± 0.06	⋯	19.70 ± 0.06	FTW-3KK	This work
62326	*i*	3.931700	19.89 ± 0.04	⋯	19.66 ± 0.04	FTW-3KK	This work
62537	*i*	3.931700	19.87 ± 0.05	⋯	19.64 ± 0.05	FTW-3KK	This work
62749	*i*	3.931700	19.99 ± 0.06	⋯	19.76 ± 0.06	FTW-3KK	This work
62961	*i*	3.931700	19.93 ± 0.06	⋯	19.70 ± 0.06	FTW-3KK	This work
63172	*i*	3.931700	19.98 ± 0.09	⋯	19.75 ± 0.09	FTW-3KK	This work
63384	*i*	3.931700	19.92 ± 0.07	⋯	19.69 ± 0.07	FTW-3KK	This work
63596	*i*	3.931700	20.04 ± 0.10	⋯	19.81 ± 0.10	FTW-3KK	This work
63808	*i*	3.931700	19.67 ± 0.24	⋯	19.44 ± 0.24	FTW-3KK	This work

Table A1
(Continued)

Time T_0 (s)	Filter	Frequency ($\times 10^{14}$ Hz)	Mag (AB)	Lim Mag (AB)	Corr Mag (AB)	Instrument	References
45272	*J*	2.400000	19.84 ± 0.34	⋯	19.75 ± 0.34	FTW-3KK	This work
45567	*J*	2.400000	19.42 ± 0.14	⋯	19.33 ± 0.14	FTW-3KK	This work
45779	*J*	2.400000	19.81 ± 0.21	⋯	19.72 ± 0.21	FTW-3KK	This work
45990	*J*	2.400000	19.59 ± 0.17	⋯	19.50 ± 0.17	FTW-3KK	This work
46202	*J*	2.400000	19.90 ± 0.26	⋯	19.81 ± 0.26	FTW-3KK	This work
46414	*J*	2.400000	20.11 ± 0.31	⋯	20.02 ± 0.31	FTW-3KK	This work
46625	*J*	2.400000	19.91 ± 0.24	⋯	19.82 ± 0.24	FTW-3KK	This work
46837	*J*	2.400000	19.48 ± 0.15	⋯	19.39 ± 0.15	FTW-3KK	This work
47048	*J*	2.400000	19.37 ± 0.13	⋯	19.28 ± 0.13	FTW-3KK	This work
47260	*J*	2.400000	19.41 ± 0.14	⋯	19.32 ± 0.14	FTW-3KK	This work
61918	*J*	2.400000	19.53 ± 0.08	⋯	19.43 ± 0.08	FTW-3KK	This work
62128	*J*	2.400000	19.68 ± 0.13	⋯	19.58 ± 0.13	FTW-3KK	This work
62340	*J*	2.400000	19.52 ± 0.08	⋯	19.43 ± 0.08	FTW-3KK	This work
62552	*J*	2.400000	19.44 ± 0.07	⋯	19.35 ± 0.07	FTW-3KK	This work
62763	*J*	2.400000	19.51 ± 0.08	⋯	19.42 ± 0.08	FTW-3KK	This work
62976	*J*	2.400000	19.44 ± 0.07	⋯	19.35 ± 0.07	FTW-3KK	This work
63187	*J*	2.400000	19.57 ± 0.08	⋯	19.48 ± 0.08	FTW-3KK	This work
63399	*J*	2.400000	19.58 ± 0.09	⋯	19.49 ± 0.09	FTW-3KK	This work
63610	*J*	2.400000	19.65 ± 0.09	⋯	19.56 ± 0.09	FTW-3KK	This work
63822	*J*	2.400000	19.72 ± 0.34	⋯	19.62 ± 0.34	FTW-3KK	This work
137884	*r*	4.811310	21.89 ± 0.07	⋯	21.58 ± 0.07	FTW-3KK	This work
144446	*r*	4.811310	22.06 ± 0.05	⋯	21.76 ± 0.05	FTW-3KK	This work
137884	*i*	3.931700	21.84 ± 0.11	⋯	21.61 ± 0.11	FTW-3KK	This work
144446	*i*	3.931700	21.85 ± 0.06	⋯	21.62 ± 0.06	FTW-3KK	This work
137898	*J*	2.400000	21.65 ± 0.27	⋯	21.56 ± 0.27	FTW-3KK	This work
144461	*J*	2.400000	21.19 ± 0.10	⋯	21.10 ± 0.10	FTW-3KK	This work
133056	*J*	2.400000	⋯	18.90	⋯	HCT	This work
291168	*r*	4.811310	⋯	21.80	⋯	HCT	This work

Note. The table includes the time since the burst ($T - T_0$) in seconds, filter or band, central frequency (in Hz), measured magnitude (in AB system), upper limits, galactic-extinction-corrected magnitude (in AB system), and observing instrument, along with references for each data point.

Table A2
Log of X-ray Observations of the X-ray Afterglow of GRB 250704B Taken Using Swift-XRT and Chandra

$T_{start} - T_0$ (s)	$T_{stop} - T_0$ (s)	Flux (10^{-11} erg cm^{-2} s^{-1})	Photon Index	$\text{Flux}_{10\text{ keV}}$ (10^{-4} mJy)	$\text{Flux}_{1\text{keV}}$ (10^{-3} mJy)
1963	2109	2.43 ± 0.54	$1.65^{+0.43}_{-0.31}$	4.97 ± 1.10	2.22 ± 0.49
2109	2214	1.41 ± 0.32	$1.72^{+0.31}_{-0.22}$	2.60 ± 0.59	1.37 ± 0.31
2214	2435	1.64 ± 0.37	$1.84^{+0.28}_{-0.20}$	2.52 ± 0.57	1.75 ± 0.39
2435	2535	1.26 ± 0.28	$1.93^{+0.33}_{-0.23}$	1.68 ± 0.37	1.43 ± 0.32
2535	2633	1.27 ± 0.28	$2.03^{+0.24}_{-0.18}$	1.41 ± 0.31	1.52 ± 0.34
2633	2718	1.44 ± 0.32	$2.12^{+0.31}_{-0.23}$	1.37 ± 0.30	1.80 ± 0.40
2718	2834	1.00 ± 0.23	$2.19^{+0.24}_{-0.18}$	0.83 ± 0.19	1.28 ± 0.29
2834	2926	1.22 ± 0.28	$2.26^{+0.24}_{-0.18}$	0.88 ± 0.20	1.61 ± 0.36
2926	3044	1.00 ± 0.22	$2.31^{+0.31}_{-0.23}$	0.64 ± 0.14	1.33 ± 0.30
3044	3159	1.05 ± 0.23	$2.25^{+0.23}_{-0.18}$	0.77 ± 0.17	1.38 ± 0.30
3159	3272	1.01 ± 0.23	$2.18^{+0.20}_{-0.15}$	0.84 ± 0.19	1.30 ± 0.30
3272	3445	0.68 ± 0.15	$2.11^{+0.24}_{-0.18}$	0.66 ± 0.15	0.84 ± 0.19
3445	3681	0.87 ± 0.15	$2.08^{+0.26}_{-0.20}$	0.89 ± 0.15	1.07 ± 0.18
7571	7832	0.50 ± 0.11	$2.04^{+0.21}_{-0.16}$	0.54 ± 0.12	0.60 ± 0.13
92,754	172,449	0.063 ± 0.019	$1.90^{+0.54}_{-0.39}$	0.088 ± 0.026	0.070 ± 0.021
177,117	193,406	0.036 ± 0.010	$1.88^{+0.59}_{-0.43}$	0.052 ± 0.015	0.039 ± 0.011
1,553,549[a]	1,573,369	< 0.003	⋯	< 0.0053	⋯

Note. Flux values (column (3)) are obtained in the 0.3–10 keV band. $\text{Flux}_{10\text{keV}}$ and $\text{Flux}_{1\text{keV}}$ are the flux densities calculated at 10 and 1 keV, respectively.
[a] Observation taken with Chandra.

Table A3
Log of Radio Data for the Radio Afterglow of GRB 250704B Taken Using VLA, MeerKAT, and uGMRT

$T - T_0$ (s)	Instrument	Energy Band	Flux (mJy)	Flux Upper Limit (mJy)	Reference
354,240	VLA	6 GHz	0.150 ± 0.005	⋯	G. Schroeder et al. (2025b)
343,872	VLA	10 GHz	0.092 ± 0.007	⋯	R. Ricci et al. (2025)
492,480	MeerKAT	1.3 GHz	0.070 ± 0.005	⋯	G. Schroeder et al. (2025c)
1,171,802.9	uGMRT	1.3 GHz	⋯	0.050	This work
1,171,620.9	uGMRT	0.65 GHz	⋯	0.114	This work

A.1. GIT

We used the GIT located at the Indian Astronomical Observatory (IAO), Hanle-Ladakh, to acquire data of the optical afterglow of GRB 250704B (T. Mohan et al. 2025). GIT is a 0.7 m wide-field, fully robotic telescope specifically designed for the study of transient astrophysical events (H. Kumar et al. 2022). The afterglow was observed in the Sloan r' and i' filters. Data were downloaded and processed in real time using the GIT data reduction pipeline. All images were preprocessed by subtracting bias and flat-fielding followed by cosmic-ray removal via the Astro-SCRAPPY (C. McCully & M. Tewes 2019) package. Astrometry was performed on the resulting images using the offline `solve-field` astrometry engine (D. Lang et al. 2010). The sources were detected using `SExtractor` (E. Bertin & S. Arnouts 1996) and cross-matched with the Pan-STARRS DR1 catalog (K. C. Chambers et al. 2016) through `vizier` to obtain the zero-point in the images. Finally, the pipeline performed point-spread function (PSF) photometry using `PSFEx` (E. Bertin 2013) to generate the PSF of the image and obtain the GRB 250704B afterglow magnitudes.

A.2. Swift-XRT

Swift-XRT began observing GRB 250704B approximately 34 minutes after the trigger and continued with multiple epochs up to 2.17 days. For the light-curve analysis, we used the publicly available results from the UK Swift Science Data Centre.[22] We adopted the unabsorbed flux and photon index (Γ) reported in the 0.3–10 keV energy range. Assuming a power-law spectrum of the form $F_\nu \propto \nu^{-\beta}$, where the spectral index $\beta = \Gamma - 1$ and Γ is the photon index, we normalized the spectrum using the unabsorbed band flux over the 0.3–10 keV range and then evaluated the corresponding flux density at 1 and 10 keV.

A.3. Chandra

We triggered Chandra through Chandra DDT (proposal No. 26409057; PI Pathak) to observe GRB 250704B. The source was observed for a single epoch at ∼18.10 days from the trigger for an exposure of 19.82 ks. We reprocessed the data to get new level-2 data through `ciao-4.15`. Since the source was not detected, we followed the `srcflux` method to determine the model-dependent upper limit and obtained flux $\leqslant 3.41 \times 10^{-15}$ erg cm^{-2} s^{-1} in the energy range of 0.5–7.0 keV. With same method discussed in the previous section, we calculated a flux density of 5.34×10^{-8} mJy at 10 keV. This research employs a list of Chandra datasets, obtained by the Chandra X-ray Observatory, contained in DOI: 10.25574/cdc.493.

[22] https://www.swift.ac.uk/xrt_live_cat/00021535/

A.4. HCT

We observed the field of GRB 250704B using the Himalayan Faint Object Spectrograph Camera mounted on the 2 m HCT at IAO, Hanle, India. Observations were carried out in J and r' bands, beginning at 2025-07-05T21:16:47.94 UT for the J band and at 2025-07-07T17:12:23.27 UT for the r' band. A total exposure time of 1170 s in the J band and 3600 s in the r' band was obtained. Standard data reduction and photometric analysis were performed using Astro-SCRAPPY, `SExtractor`, the offline astrometry.net algorithm, and `PSFEx`, as in the case of GIT. The magnitudes are calibrated against Pan-STARRS DR1 for r' band and against the Two Micron All Sky Survey (2MASS) catalog (M. F. Skrutskie et al. 2006) for the J band. The derived upper limits are listed in Table A1.

A.5. Keck I

We observed GRB 250704B with MOSFIRE mounted on the 10 m Keck I telescope (PI Kasliwal; PROGID: C348) and acquired J-band imaging of the afterglow. The observations started at 08:55 UT on 2025 July 9 and consisted of five sets of box-9 dithered images with 11 s exposures and three coadds each. We used standard reduction methods to coadd the images and used the 2MASS catalog to calibrate our photometry. We detect a source close to the 3σ limit of our observations at $J = 24.4 \pm 0.2$ mag (AB).

Additionally, we observed GRB 250704B with the Low-Resolution Imaging Spectrometer (Oke et al. 1995) on the Keck I telescope. Observations started at 10:20 UT on 2025 July 24 and consisted of a series of 20 30 s exposures using the d680 dichroic, obtaining simultaneous observations in the V and I filters. We do not find a source at the position of the afterglow.

A.6. Blanco

We obtained four epochs of observations with the Blanco telescope between July 5 and July 8. The first epoch included imaging in the *ugriz* filters, the second and third epochs were obtained in *riz*, and the last epoch (July 8) was taken in the r band.

A.7. Fraunhofer Telescope

We observed with the 3kk instrument mounted on FTW using the r, i, and J bands (F. Lang-Bardl et al. 2016). We acquired four epochs of data on 2025-07-04 20:50:45, 2025-07-05 01:28:10, 2025-07-05 22:34:31, and 2025-07-06 00:23:53 UTC (M. Busmann et al. 2025). Each night two epochs were acquired, one at the beginning of the night and one at the end. The first three epochs were taken with 10×180 s exposures, and the last epoch was taken with 30×180 s exposures. We calibrate the J-band observations against the 2MASS catalog

and the r and i band against the Pan-STARRS1 catalog. We detect the afterglow in all epochs.

A.8. Palomar 200-inch Telescope

We use the the Wide-field Infrared Camera (WIRC; J. C. Wilson et al. 2003) on the Palomar 200-inch telescope using the near-infrared J and K_s bands. We acquired three epochs of WIRC data on 2025 July 04–06. The observations consisted of three sets of box-9 dithered images of 45 s and one coadd for J band and 3 s and 10 coadds for K_s band. We followed standard reduction techniques and calibrated against 2MASS. We detect the afterglow in the images in the first and second epochs, but not in the third epoch.

A.9. Palomar 60-inch Telescope

We acquired images with the Spectral Energy Distribution Machine (N. Blagorodnova et al. 2018) on 2025 July 04 and 05. The first epoch was automatically scheduled through our program responding to Einstein Probe events. Our second epoch was in response to the afterglow detection. We follow standard reduction methods and calibrate against Pan-STARRS (C. Fremling et al. 2016).

A.10. uGMRT

We observed the field of GRB 250704B with the wideband receiver back end of the upgraded GMRT (uGMRT) in two frequency bands: band 4 (central frequency 750 MHz, bandwidth 400 MHz) and band 5 (central frequency 1260 MHz, bandwidth 400 MHz) on 2025 July 16 and 17, respectively (48_059; PI: Eappachen). The raw data were downloaded in the `FITS` format and converted to the `CASA` (Team CASA et al. 2022) measurement set format. Then, the data were calibrated and imaged using the automated continuum imaging pipeline `CASA-CAPTURE` (R. Kale & C. H. Ishwara-Chandra 2021). Eight rounds of self-calibration were done within each pipeline run. Both the band 4 and band 5 observations in both epochs did not yield detections, and the upper limit values listed in Table A3 are the 3 $\times$ rms value in a large circle (of radius $\sim$20$\times$ resolution at the respective band) centered at the location of GRB 250704B, in the residual image.

A.11. Other Public Data

We collected the photometry circulated through GCN on this target (see Table A1), which spans from g band to J band.

Appendix B
Corner Plot of Structured Jet Model

For completeness, Figure B1 shows the corner plot of the posterior distributions of the parameters obtained from our off-axis structured jet modeling (see Section 5.2).

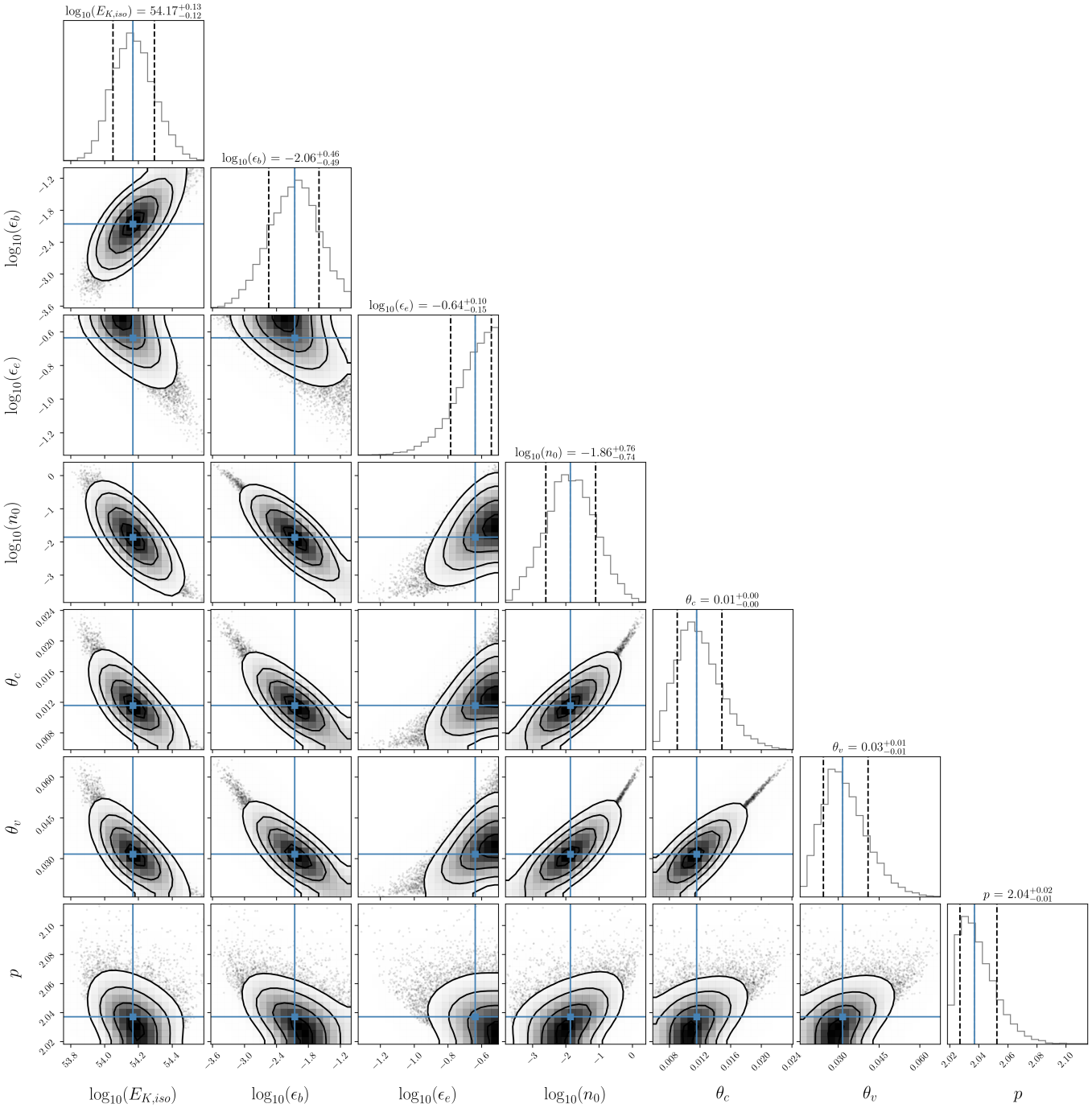

Figure B1. Posterior distribution of physical parameters for model fitted using `jetsimpy` with a structured jet interacting with the ISM medium and `MultiNest`. The model is fit for the $\log_{10}(E_{K,\rm iso})$, $\log_{10}(\epsilon_b)$, $\log_{10}(\epsilon_e)$, $\log_{10}(n_0)$, θ_c, θ_v, and p parameters. The histogram shows the 16th, 50th, and 84th percentiles of the probability distribution.

Appendix C
Energy Injection Modeling

In this appendix we explore models including energy injection.

The presence of long plateaus in GRB afterglows is often attributed to continued energy injection by some central engine, for instance, by a magnetar (B. Zhang & P. Mészáros 2001; B. D. Metzger et al. 2008; A. Rowlinson et al. 2013). To test this scenario, we used the `afterglowpy` package, where the energy injection is parameterized as

$$L(t) = L_0\left(\frac{t}{t_0}\right)^{-q}, \tag{C1}$$

with L_0 the luminosity of energy injection, t_0 fixed to 1 ks by default, and q the power-law index of energy injection (G. Ryan et al. 2020, 2024). An additional parameter, t_s, specifies the time in the source frame at which the injection ceases.

In our modeling, we adopted $q = 0$, which corresponds to a nearly constant luminosity injection from the central engine over the timescale t_s, followed by a sudden termination when the central engine collapses to a black hole. Such constant injection naturally explains the shallow decay or plateau phase commonly observed in many GRB afterglows (B. Zhang & P. Mészáros 2001; Z. G. Dai & T. Lu 1998). For the dynamics of the jet, we assumed a relativistic top-hat jet propagating in a uniform ISM, with free parameters $E_{K,\rm iso}$, ϵ_b, n_0, θ_c, θ_v, and p.

Using the same sampling method described in the Section 5.2, we obtained the posterior distributions summarized in Table C1. The inferred light curve for the best-fit model overlaid on the observed data is shown in Figure C1. From the best-fit values, we infer an isotropic kinetic energy of $E_{K,\rm iso} \sim 10^{51}$ erg, implying a radiative efficiency exceeding 80%. The model favors a jet with a core angle of 2.4°, viewed almost on-axis. We find a characteristic time of $t_s \sim 1$ ks in source frame, suggesting that up to this epoch the central engine remains active, continuously injecting energy into the jet.

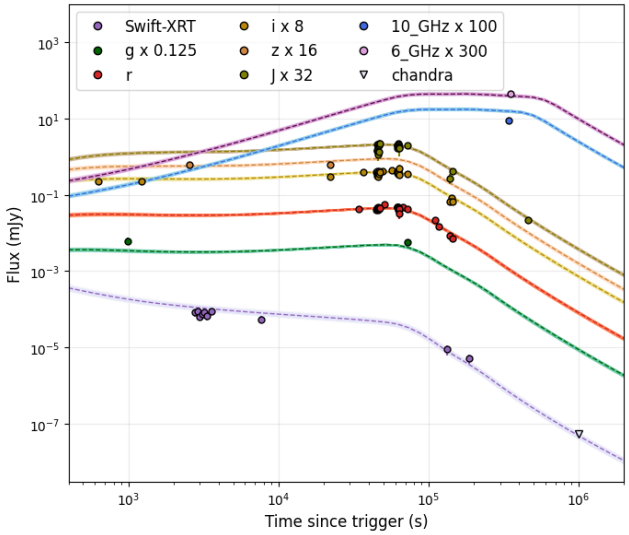

Figure C1. We modeled the multiband afterglow light curves of GRB 250704B using `afterglowpy`, assuming a relativistic structured jet with a top-hat profile propagating into a uniform-density ISM, and incorporating a constant energy injection rate. Dotted lines show the best-fit light curves, and shaded regions mark the 3σ uncertainties.

Table C1
Summary of the Priors and Posteriors for the Model Parameters Obtained from `MultiNest` Fitting of Energy Injection Model Implemented Using `afterglowpy`

Parameter	Unit	Prior Type	Parameter Bound	Posterior Value
$\log_{10}(E_{K,\rm iso})$	erg	uniform	[48, 53]	$51.04^{+0.03}_{-0.03}$
$\log_{10}(\epsilon_b)$	⋯	uniform	[−5, −1]	$-2.58^{+0.08}_{-0.06}$
$\log_{10}(\epsilon_e)$	⋯	uniform	[−3, −0.1]	$-0.13^{+0.02}_{-0.04}$
$\log_{10}(n_0)$	$\rm cm^{-3}$	uniform	[−4, 1]	$-0.96^{+0.03}_{-0.04}$
θ_c	rad	log-uniform	$[10^{-4}, 0.2]$	$0.044^{+0.001}_{-0.001}$
θ_v	rad	log-uniform	$[10^{-4}, 0.2]$	$0.003^{+0.001}_{-0.001}$
p	⋯	uniform	[2.001, 3]	$2.06^{+0.007}_{-0.004}$
$\log_{10}(L_0)$	$\rm erg\ s^{-1}$	uniform	[43, 51]	$45.28^{+0.028}_{-0.023}$
$\log_{10}(t_s)$	s	uniform	[2, 6]	$3.06^{+0.09}_{-0.10}$
χ	⋯	⋯	⋯	1

The inferred CBM density is $n \sim 0.1\ \rm cm^{-3}$, about an order of magnitude larger than the range typically expected for magnetar-powered afterglows, 10^{-3} to $10^{-2}\ \rm cm^{-3}$ (A. Rowlinson et al. 2013), where lower densities are generally more favorable for efficient energy injection. The microphysical parameters are $\epsilon_e = 0.74 \pm 0.07$, $\epsilon_b \sim 0.003$, and $p = 2.06 \pm 0.01$. The unusually high value of ϵ_e suggests a strong inverse Compton cooling (R. Sari & A. A. Esin 2001), which is not included in our present model. On the other hand, if we fix ϵ_e to the typical value of 0.1, the fit quality degrades significantly and requires an unrealistically large external density, again inconsistent with the magnetar scenario.

Overall, we find that while the constant energy injection model is capable of reproducing plateau features in GRB afterglows, fitting the afterglow of GRB 250704B within this framework requires implausible values for physical parameters such as ϵ_e or n_0. In contrast, the off-axis structured jet model does not suffer from these shortcomings and is therefore preferred for explaining the afterglow of GRB 250704B.

ORCID iDs

Vishwajeet Swain https://orcid.org/0000-0002-7942-8477
Tomás Ahumada https://orcid.org/0000-0002-2184-6430
Sameer K. Patil https://orcid.org/0009-0002-8110-0515
Yogesh Wagh https://orcid.org/0000-0002-5890-9298
Varun Bhalerao https://orcid.org/0000-0002-6112-7609
Ehud Nakar https://orcid.org/0000-0002-4534-7089
Mansi Kasliwal https://orcid.org/0000-0002-5619-4938
Xander J. Hall https://orcid.org/0000-0002-9364-5419
Malte Busmann https://orcid.org/0009-0001-0574-2332
Utkarsh Pathak https://orcid.org/0009-0002-7897-6110
Shreya Anand https://orcid.org/0000-0003-3768-7515
Viraj Karambelkar https://orcid.org/0000-0003-2758-159X
Igor Andreoni https://orcid.org/0000-0002-8977-1498
G. C. Anupama https://orcid.org/0000-0003-3533-7183
Anuraag Arya https://orcid.org/0009-0007-9244-191X
Arvind Balasubramanian https://orcid.org/0000-0003-0477-7645
Sudhanshu Barway https://orcid.org/0000-0002-3927-5402
Jonathan Carney https://orcid.org/0000-0001-8544-584X
Michael Coughlin https://orcid.org/0000-0002-8262-2924
D. Eappachen https://orcid.org/0000-0001-7841-0294

James Freeburn https://orcid.org/0009-0006-7990-0547
Daniel Gruen https://orcid.org/0000-0003-3270-7644
Tanishk Mohan https://orcid.org/0009-0001-4683-388X
Brendan O'Connor https://orcid.org/0000-0002-9700-0036
Antonella Palmese https://orcid.org/0000-0002-6011-0530
D. K. Sahu https://orcid.org/0000-0002-6688-0800
Aditya Pawan Saikia https://orcid.org/0009-0005-2987-0688
Nikhil Sarin https://orcid.org/0000-0003-2700-1030
Gokul Srinivasaragavan https://orcid.org/0000-0002-6428-2700
Hitesh Tanenia https://orcid.org/0009-0008-6644-5412

References

Acciari, V. A., Ansoldi, S., Antonelli, L. A., et al. 2021, ApJ, 908, 90
Ackermann, M., Asano, K., Atwood, W. B., et al. 2010, ApJ, 716, 1178
Ahumada, T., Singer, L. P., Anand, S., et al. 2021, NatAs, 5, 917
An, J., Malesani, D. B., Xu, D., et al. 2025a, GCN, 40966, 1
An, J., Martin-Carrillo, A., Malesani, D. B., et al. 2025b, GCN, 40993, 1
Ascenzi, S., Oganesyan, G., Salafia, O. S., et al. 2020, A&A, 641, A61
Astropy Collaboration, Price-Whelan, A. M., Lim, P. L., et al. 2022, ApJ, 935, 167
Astropy Collaboration, Price-Whelan, A. M., Sipőcz, B. M., et al. 2018, AJ, 156, 123
Astropy Collaboration, Robitaille, T. P., Tollerud, E. J., et al. 2013, A&A, 558, A33
Bertin, E., 2013 PSFEx: Point Spread Function Extractor, Astrophysics Source Code Library, ascl:1301.001
Bertin, E., & Arnouts, S. 1996, A&AS, 117, 393
Blagorodnova, N., Neill, J. D., Walters, R., et al. 2018, PASP, 130, 035003
Buchner, J., Georgakakis, A., Nandra, K., et al. 2014, A&A, 564, A125
Busmann, M., Hall, X., O'Connor, B., Gruen, D., & Palmese, A. 2025, GCN, 40974, 1
Team CASA, Bean, B., Bhatnagar, S., et al. 2022, PASP, 134, 114501
Chambers, K. C., Magnier, E. A., Metcalfe, N., et al. 2016, arXiv:1612.05560
Dai, Z. G., & Lu, T. 1998, A&A, 333, L87
Eichler, D., & Levinson, A. 2004, ApJL, 614, L13
Fong, W., Berger, E., Margutti, R., & Zauderer, B. A. 2015, ApJ, 815, 102
Fraija, N., Dainotti, M. G., Levine, D., Kamenetskaia, B. B., & Galvan-Gamez, A. 2023, ApJ, 958, 126
Fraija, N., Galvan-Gamez, A., Betancourt Kamenetskaia, B., et al. 2022, ApJ, 940, 189
Fraija, N., Lee, W. H., Veres, P., & Barniol Duran, R. 2016, ApJ, 831, 22
Fraija, N., Veres, P., Betancourt Kamenetskaia, B., et al. 2024, MNRAS, 534, 3783
Frederiks, D., Lysenko, A., Ridnaia, A., et al. 2025, GCN, 40972, 1
Fremling, C., Sollerman, J., Taddia, F., et al. 2016, A&A, 593, A68
Fruscione, A., McDowell, J. C., Allen, G. E., et al. 2006, SPIE, 6270, 62701V
Ghirlanda, G., Salafia, O. S., Paragi, Z., et al. 2019, Sci, 363, 968
Gillanders, J. H., Huber, M., Chambers, K. C., et al. 2025, GCN, 40958, 1
Goldstein, A., Cleveland, W. H., & Kocevski, D. 2023, Fermi Gamma-ray Data Tools: v2.0.0, GitHub, https://github.com/USRA-STI/gdt-fermi
Govreen-Segal, T., & Nakar, E. 2023, MNRAS, 524, 403
Govreen-Segal, T., & Nakar, E. 2024, MNRAS, 531, 1704
Granot, J., Gill, R., Guetta, D., & De Colle, F. 2018, MNRAS, 481, 1597
Granot, J., Panaitescu, A., Kumar, P., & Woosley, S. E. 2002, ApJL, 570, L61
Granot, J., & Sari, R. 2002, ApJ, 568, 820
Guidorzi, C., Mundell, C. G., Harrison, R., et al. 2014, MNRAS, 438, 752
Hascoët, R., Daigne, F., Mochkovitch, R., & Vennin, V. 2012, MNRAS, 421, 525
He, H.-N., Wu, X.-F., Toma, K., Wang, X.-Y., & Mészáros, P. 2011, ApJ, 733, 22
Kale, R., & Ishwara-Chandra, C. H. 2021, ExA, 51, 95
Kann, D. A., Agayeva, S., Aivazyan, V., et al. 2023, ApJL, 948, L12
Kasliwal, M. M., Cannella, C., Bagdasaryan, A., et al. 2019, PASP, 131, 038003
Knust, F., Greiner, J., van Eerten, H. J., et al. 2017, A&A, 607, A84
Kouveliotou, C., Meegan, C. A., Fishman, G. J., et al. 1993, ApJL, 413, L101
Kozyrev, A. S., Golovin, D. V., Litvak, M. L., et al. 2025, GCN, 41050, 1
Kumar, H., Bhalerao, V., Anupama, G. C., et al. 2022, AJ, 164, 90
Kumar, P. 1999, ApJL, 523, L113
Lamb, G. P., Tanvir, N. R., Levan, A. J., et al. 2019, ApJ, 883, 48
Lang, D., Hogg, D. W., Mierle, K., Blanton, M., & Roweis, S. 2010, AJ, 139, 1782
Lang-Bardl, F., Bender, R., Goessl, C., et al. 2016, SPIE, 9908, 990844
Levan, A. J., Gompertz, B. P., Salafia, O. S., et al. 2024, Natur, 626, 737
Li, A., Cheng, Y. H., Zhou, C., et al. 2025, GCN, 40956, 1
Li, W. X., Xue, S. J., Andrews, M., et al. 2025, GCN, 40975, 1
Liu, X., An, J., Zhu, Z. P., et al. 2025, GCN, 40965, 1
Lloyd-Ronning, N. M., & Zhang, B. 2004, ApJ, 613, 477
Makhathini, S., Mooley, K. P., Brightman, M., et al. 2021, ApJ, 922, 154
Malesani, D. B., Eyles-Ferris, R., Corcoran, G., et al. 2025, GCN, 40945, 1
Martin-Carrillo, A., Malesani, D. B., Liu, X., et al. 2025, GCN, 40971, 1
Maxham, A., & Zhang, B. 2009, ApJ, 707, 1623
McCully, C., & Tewes, M., 2019 Astro-SCRAPPY: Speedy Cosmic Ray Annihilation Package in Python, Astrophysics Source Code Library, ascl:1907.032
Mészáros, P. 2002, ARA&A, 40, 137
Mészáros, P. 2006, RPPh, 69, 2259
Mészáros, P., & Rees, M. J. 1997, ApJ, 476, 232
Metzger, B. D., Quataert, E., & Thompson, T. A. 2008, MNRAS, 385, 1455
Mohan, T., Swain, V., Saikia, A. P., et al. 2025, GCN, 40962, 1
Mooley, K. P., Anderson, J., & Lu, W. 2022, Natur, 610, 273
Mooley, K. P., Deller, A. T., Gottlieb, O., et al. 2018, Natur, 561, 355
Nakar, E., & Piran, T. 2021, ApJ, 909, 114
Norris, J. P., & Bonnell, J. T. 2006, ApJ, 643, 266
Norris, J. P., Gehrels, N., & Scargle, J. D. 2010, ApJ, 717, 411
O'Connor, B., Beniamini, P., & Gill, R. 2024, MNRAS, 533, 1629
O'Connor, B., Beniamini, P., & Kouveliotou, C. 2020, MNRAS, 495, 4782
O'Connor, B., Troja, E., Ryan, G., et al. 2023, SciA, 9, eadi1405
Oganesyan, G., Ascenzi, S., Branchesi, M., et al. 2020, ApJ, 893, 88
Panaitescu, A. 2020, ApJ, 895, 39
Panaitescu, A., & Vestrand, W. T. 2008, MNRAS, 387, 497
Rastinejad, J. C., Gompertz, B. P., Levan, A. J., et al. 2022, Natur, 612, 223
Rees, M. J., & Meszaros, P. 1992, MNRAS, 258, 41
Resmi, L., Schulze, S., Ishwara-Chandra, C. H., et al. 2018, ApJ, 867, 57
Ricci, R., Becerra, R. L., Troja, E. & ERC BHianca Team 2025, GCN, 41046, 1
Rowlinson, A., O'Brien, P. T., Metzger, B. D., Tanvir, N. R., & Levan, A. J. 2013, MNRAS, 430, 1061
Ryan, G., van Eerten, H., Piro, L., & Troja, E. 2020, ApJ, 896, 166
Ryan, G., van Eerten, H., Troja, E., et al. 2024, ApJ, 975, 131
Sari, R. 1997, arXiv:astro-ph/9706078
Sari, R., & Esin, A. A. 2001, ApJ, 548, 787
Sari, R., Piran, T., & Halpern, J. P. 1999, ApJL, 519, L17
Sari, R., Piran, T., & Narayan, R. 1998, ApJL, 497, L17
Schlafly, E. F., & Finkbeiner, D. P. 2011, ApJ, 737, 103
Schlegel, D. J., Finkbeiner, D. P., & Davis, M. 1998, ApJ, 500, 525
Schneider, B., Becerra, R. L., Antier, S., et al. 2025, GCN, 40942, 1
Schroeder, G., Fong, W.-f., Kilpatrick, C. D., et al. 2025a, ApJ, 982, 42
Schroeder, G., Rastinejad, J., Fong, W., & Laskar, T. 2025b, GCN, 41038, 1
Schroeder, G., Rhodes, L., Fong, W., Laskar, T., & Berger, E. 2025c, GCN, 41060, 1
Shimizu, Y., Yoshida, A., Sakamoto, T., et al. 2025, GCN, 41025, 1
Skrutskie, M. F., Cutri, R. M., Stiening, R., et al. 2006, AJ, 131, 1163
Srinivasaragavan, G. P., O'Connor, B., Cenko, S. B., et al. 2023, ApJL, 949, L39
SVOM/GRM Team, Wang, C.-W., Zheng, S.-J., et al. 2025, GCN, 40940, 1
Troja, E., Castro-Tirado, A. J., Becerra González, J., et al. 2019a, MNRAS, 489, 2104
Troja, E., Fryer, C. L., O'Connor, B., et al. 2022, Natur, 612, 228
Troja, E., Ryan, G., Piro, L., et al. 2018, NatCo, 9, 4089
Troja, E., Sakamoto, T., Cenko, S. B., et al. 2016, ApJ, 827, 102
Troja, E., van Eerten, H., Ryan, G., et al. 2019b, MNRAS, 489, 1919
Volnova, A., Pozanenko, A., Klunko, E., et al. 2025, GCN, 41024, 1
Wang, C.-W., Xiong, S.-L., Li, C.-K., Zheng, C. & Insight-HXMT Team 2025, GCN, 40978, 1
Wang, H., Dastidar, R. G., Giannios, D., & Duffell, P. C. 2024, ApJS, 273, 17
Wang, X.-G., Zhang, B., Liang, E.-W., et al. 2015, ApJS, 219, 9
Wilson, J. C., Eikenberry, S. S., Henderson, C. P., et al. 2003, Proc. SPIE, 4841, 451
Xin, L. P., Li, H. L., Qiu, Y. L., et al. 2025, GCN, 40960, 1
Yang, J., Ai, S., Zhang, B.-B., et al. 2022, Natur, 612, 232
Yang, Y.-H., Passaleva, N., Becerra, R. L., et al. 2025, GCN, 40970, 1
Zhang, B., & Mészáros, P. 2001, ApJL, 552, L35
Zhang, B. B., Liu, Z. K., Peng, Z. K., et al. 2021, NatAs, 5, 911
Zhang, W., & MacFadyen, A. 2009, ApJ, 698, 1261